This is a repository copy of *Finite thickness of shear bands in frictional viscoplasticity and implications for lithosphere dynamics*.

Article:

Finite Thickness of Shear Bands in Frictional Viscoplasticity and Implications for Lithosphere Dynamics

Thibault Duretz[1,2] [ID] , **René de Borst[3]** [ID] , and **Laetitia Le Pourhiet[4]** [ID]

[1]Géosciences Rennes UMR 6118, Univ Rennes, CNRS, Rennes, France, [2]Institut des Sciences de la Terre, University of Lausanne, Lausanne, Switzerland, [3]Department of Civil and Structural Engineering, University of Sheffield, Sheffield, UK, [4]Institut des Sciences de la Terre de Paris (iSTeP), Sorbonne Universités, UPMC Univ Paris 06, CNRS, Paris, France

Abstract Permanent deformations in the lithosphere can occur in the brittle as well as in the ductile domain. For this reason, the inclusion of viscous creep and frictional plastic deformation is essential for geodynamic models. However, most currently available models of frictional plasticity are rate independent and therefore do not incorporate an internal length scale, which is an indispensible element for imposing a finite width of localized shear zones. Therefore, in computations of localization, either analytical or numerical, resulting shear zone widths tend to zero. In numerical computations, this manifests itself in a severe mesh sensitivity. Moreover, convergence of the global iterative procedure to solve the nonlinear processes is adversely affected, which negatively affects the reliability and the quality of predictions. The viscosity that is inherent in deformation processes in the lithosphere can, in principle, remedy this mesh sensitivity. However, elasto-viscoplastic models that are commonly used in geodynamics assume a series arrangement of rheological elements (Maxwell-type approach), which does not introduce an internal length scale. Here, we confirm that a different rheological arrangement that puts a damper in parallel to the plastic slider (Kelvin-type approach) introduces an internal length scale. As a result, pressure and strain and strain rate profiles across the shear bands converge to finite values upon decreasing the grid spacing. We demonstrate that this holds for nonassociated plasticity with constant frictional properties and with material softening with respect to cohesion. Finally, the introduction of Kelvin-type viscoplasticity also significantly improves the global convergence of nonlinear solvers.

1. Introduction

Shear localization refers to the phenomenon of the concentration of strains in narrow zones when the applied load exceeds a certain threshold level. It occurs in virtually all materials (Nadai, 1931), takes place at all spatial and temporal scales within the lithosphere, and manifests itself through phenomena, which are widespread in rocks, for example, faults, shear zones, and shear bands. The localization of strains is observed in lithospheric domains where stress levels are controlled mainly by either the temperature or the strain rate (viscous creep, ductile mode) or the pressure (frictional plasticity, brittle mode). While the mechanisms that govern strain localization in the ductile mode are still being discussed (Bercovici et al., 2001; Duretz & Schmalholz, 2015; Précigout & Gueydan, 2009; Thielmann & Kaus, 2012), those acting in the brittle mode, particularly in the realm of nonassociated plasticity, are fairly well established (Poliakov et al., 1994; Rudnicki & Rice, 1975).

For the purpose of geodynamic modeling, accounting for plasticity is mandatory to capture the self-consistent generation of tectonic plates (e.g., Tackley, 2000) and the development of fault zones (e.g., Gerbault et al., 1998; Poliakov et al., 1993). However, the physical processes within shear bands, which control their width, are often considered to be beyond the scope of current geodynamic models. Hence, for sake of simplicity, strain localization is often induced by a priori-defined strain-softening functions (Buck & Lavier, 2001; Buiter et al., 2006; Döhmann et al., 2019; Huismans & Beaumont, 2002; Lavier et al., 1999), which are meant to take into account the role of complex thermo-hydro-chemico-mechanical interactions within faults in a phenomenological sense.

Since geodynamic models need to deal primarily with large deviatoric static strains, most models rely on the incompressible Stokes equations (e.g., Gerya & Yuen, 2003; Fullsack, 1995; Tackley, 2000). Typically,

viscoplasticity is used to describe the rheological behavior of geomaterials under these conditions, treating them as highly viscous fluids that can locally undergo plastic flow if a yield criterion is met (Willett, 1992). Many geodynamic models neglect the role of elasticity and can therefore not capture the effects of elastic unloading, which can be pivotal in the proper description of progressive shear-band development. Multidimensional stress states in geodynamics are typically captured using pressure-dependent yield functions like Drucker-Prager or Mohr-Coulomb (Moresi et al., 2007; Popov & Sobolev, 2008).

For most rocks, the angle of internal friction is relatively large in the steady state, around 30° or more (Byerlee, 1978). On the other hand, the magnitude of the dilatancy angle, which controls the amount of plastic volumetric change for a given amount of plastic shearing, is usually much lower, at most 10–15° at the onset of shear banding (Vermeer & de Borst, 1984), tending to zero for progressively increasing deformations. The latter observation ties in with the common use of the incompressible Stokes equations for these applications. The nearly incompressible nature of the plastic flow in combination with the strong frictional character of geomaterials renders the plasticity models nonassociated.

Both the introduction of strain softening and the use of nonassociated flow rules in pressure-dependent plasticity models yield mesh-dependent results and often exhibit an erratic and unsatisfactory convergence behavior of the equilibrium-searching iterative procedure (Spiegelman et al., 2016). The underlying reason is that the introduction of cohesion softening or of a nonassociated flow rule has a mechanically destabilizing influence. Indeed, both for cohesion softening (Read & Hegemier, 1984) and for nonassociated flow (Rudnicki & Rice, 1975) not only loss of mechanical stability can be induced but, worse, also loss of ellipticity. This mathematical condition is the basic cause of the frequently observed mesh dependence, which occurs in computations of materials that have constitutive laws that are equipped with this kind of behavior. It has also been shown that under such conditions convergence of the incremental-iterative solution procedure deteriorates with increasing mesh refinement (de Borst et al., 2012).

For nonassociated flow, loss of ellipticity can happen even if the material is still hardening and simulations have shown that global structural softening can then take place (de Borst, 1988; Le Pourhiet, 2013; Sabet & de Borst, 2019). It occurs at more and more positive hardening rates when the difference increases between the angles of internal friction and dilatancy.

It is emphasized that the fundamental, mechanical-mathematical cause of these numerical problems is loss of ellipticity. Loss of ellipticity can cause the initial value problem to become ill posed, which makes that solutions no longer continuously depend on the initial and boundary conditions. Numerical solutions then become meaningless, since they are fully dependent on the discretization, with respect to the fineness of the mesh and also with respect to the direction of the grid lines (Jirašek & Grassl, 2008; Sluys & Berends, 1998). This holds for any discretization method, including meshless methods (Pamin et al., 2003), and also, adaptive mesh refinement is severely biased (Perić et al., 1994).

Unless a plasticity model that incorporates cohesion softening or nonassociated flow is equipped with an internal length scale, it will lose ellipticity and hence suffer from mesh sensitivity, at some loading stage. Yet most plasticity models that have been used so far in long-term tectonics do not incorporate an internal length scale. Such models, while ubiquitous in geophysics, geomechanics, and engineering, are based on the assumption that the mechanical behavior in a point is representative for a small but finite volume surrounding it. This assumption is often correct but fails for highly localized deformations, like fault movement or shear bands. In the presence of strain weakening or nonassociated flow, local stress-strain relations have to be enriched to properly take into account the physical processes that occur at small length scales. A range of possibilities has been proposed to remedy this deficiency (de Borst et al., 1993), including Cosserat plasticity (Mühlhaus & Vardoulakis, 1987; Stefanou et al., 2019), nonlocal plasticity (Bažant & Jirasek, 2002), and gradient plasticity (de Borst & Mühlhaus, 1992). Unfortunately, all these possible solutions come with disadvantages. Obviously, they share the need to specify additional boundary conditions, which are often not easily understood from the physics. Other disadvantages are the introduction of additional degrees of freedom, as in Cosserat or gradient models, or they can result in fully populated, nonbanded, and nonsymmetric stiffness matrices (nonlocal models).

For geodynamic applications, the inclusion of a deformation-limiting viscosity, which has been tailored for modeling the deformation of crystalline solids (Needleman, 1988; Peirce et al., 1983), represents an alternative to nonlocal rheological models. It is emphasized though that not all visco-elasto-plastic rheologies solve
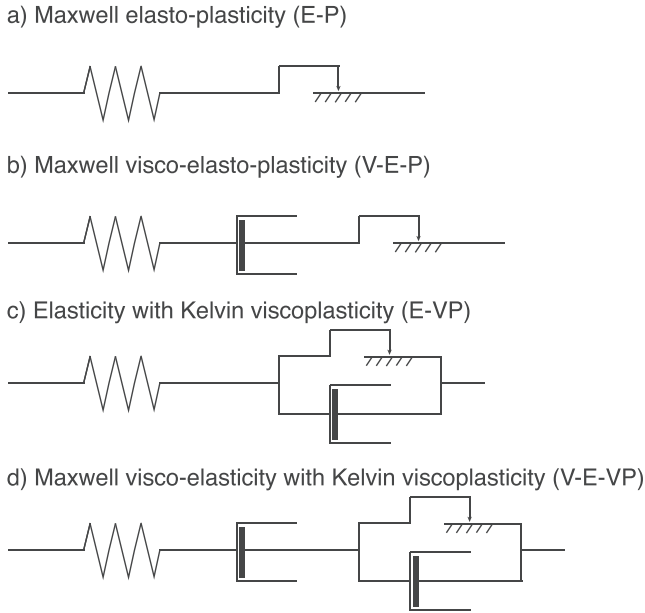
a) Maxwell elasto-plasticity (E-P)

b) Maxwell visco-elasto-plasticity (V-E-P)

c) Elasticity with Kelvin viscoplasticity (E-VP)

d) Maxwell visco-elasticity with Kelvin viscoplasticity (V-E-VP)

Figure 1. Investigated rheological models for deformation of the lithosphere: (a) Maxwell elasto-plastic model, (b) Maxwell visco-elasto-plastic model, (c) elastic model coupled to a Kelvin viscoplastic element, and (d) Maxwell visco-elastic model coupled to a Kelvin viscoplastic element.

the issue of mesh dependence and that a pure series arrangement of the rheological elements (Maxwell-type approach; see Figure 1b), for instance, does not introduce a length scale and therefore does not remove the mesh-dependence issue. By contrast, a viscoplastic model that relies on the introduction of a rate-limiting viscosity in a parallel arrangement with a plastic slider (Kelvin-type viscoplasticity, Figure 1c; Perzyna, 1966) does introduce a length scale and can provide mesh-independent numerical solutions (Dias da Silva, 2004; Niazi et al., 2013; Sluys & de Borst, 1992; Wang et al., 1996). Although a Kelvin-type viscoplasticity rheology has been used in tectonic modeling studies before (e.g., Hansen, 2003; Regenauer-Lieb et al., 2018; Yin et al., 2018), the consequences have largely remained unexplored.

Herein, we will numerically study strain localization using nonassociated Drucker-Prager plasticity, which captures the first-order behavior of the frictional lithosphere (Lemiale et al., 2008; Moresi et al., 2007; Kaus, 2010). We first illustrate the problem of mesh dependence using rate-independent plasticity. Then, we introduce a Kelvin-type rate-dependent viscoplastic formulation and demonstrate that the computed shear bands are mesh independent, even when strain softening is also introduced. We analyze the pressure, strain, and strain rate profiles across the shear bands as well as their evolution. Finally, we discuss the implications of using viscoplasticity for modeling in geodynamics.

2. Constitutive Models

In the remainder, we consider three rheological models. The first model is a standard, rate-independent elasto-plastic model (E-P), depicted in Figure 1a, and, assuming small strains, it can be characterized by an additive decomposition of the strain rate into an elastic component and a plastic component:

$$\dot{\epsilon} = \dot{\epsilon}^{\mathrm{e}} + \dot{\epsilon}^{\mathrm{p}}, \tag{1}$$

where the subscripts e and p denote elastic and plastic components, respectively. The deviatoric elastic strain $\epsilon^{\mathrm{e}\prime}$ relates to the deviatoric stress τ as follows:

$$\epsilon^{\mathrm{e}\,\prime} = \frac{\tau}{2G}, \tag{2}$$

where G represents the shear modulus, which is kept constant for simplicity.

Plastic deformations arise when the yield function

$$F = \sqrt{J_2} - C\cos(\phi) - P\sin(\phi) \tag{3}$$

attains a zero value, with C and ϕ the cohesion and the angle of internal friction, respectively. $J_2 = \frac{1}{2}\left(\tau_{xx}^2 + \tau_{yy}^2 + \tau_{zz}^2\right) + \tau_{xy}^2$ is the second invariant of the deviatoric stresses $\tau_{xx}, \tau_{yy}, \tau_{zz}, \mathrm{and}\, \tau_{xy}$, and $P = -\frac{1}{3}\left(\sigma_{xx} + \sigma_{yy} + \sigma_{zz}\right)$ is the mean stress, defined as negative in tension. When cohesion hardening or softening is incorporated, the hardening/softening modulus takes the form:

$$h = \frac{\mathrm{d}C}{\mathrm{d}\epsilon^{\mathrm{p}}}, \tag{4}$$

where ϵ^{p} is the accumulated equivalent plastic strain according to the strain-hardening hypothesis and is formulated as

$$\epsilon^{\mathrm{p}} = \int \sqrt{\frac{2}{3}\left(\dot{\epsilon}^{\mathrm{p}}\right)^T \dot{\epsilon}^{\mathrm{p}}}\mathrm{d}t. \tag{5}$$

During continued plastic flow, $F = 0$ and the deviatoric strain rates are assumed to be derivable from a plastic potential function Q:

$$\dot{\epsilon}^{\mathrm{p}} = \dot{\lambda}\frac{\partial Q}{\partial \sigma}, \tag{6}$$

Table 1
List of Parameters Relative to the Different Tests Presented in This Study

Parameter	Model 1 E-P	Model 2 E-VP	Model 3 V-E-P	Model 4 E-VP soft.	Model Crust 1	Model Crust 2
L_x (m)	1	1	1	1	1.0×10^4	2×10^4
L_y (m)	0.7	0.7	0.7	0.7	0.685×10^4	10^4
$\Delta\epsilon_{\mathrm{BC}}$ (—)	$5 \times 10^{-6*}$	5×10^{-6}	$5 \times 10^{-6*}$	5×10^{-6}	2×10^{-5}	5×10^{-5}
Δt (s)	—	10^4	10^4	10^4	10^8	10^{10}
P_c (Pa)	0	0	0	0	0	50×10^6
C (Pa)	1.74×10^{-4}	1.74×10^{-4}	1.74×10^{-4}	1.74×10^{-4}	1.75×10^7	10^{7**}
h (Pa)	0	0	0	-10^{-2}	-7×10^7	-1.5×10^7
K (Pa)	2	2	2	2	2×10^{10}	2×10^{10}
G (Pa)	1	1	1	1	10^{10}	10^{10}
η (Pa·s)	—	—	2.5×10^5	—	—	—
η^{VP} (Pa·s)	—	2.5×10^2	—	2.5×10^5	1×10^{17}	3×10^{18}

*In Models 1 and 3, the strain increment may vary with time to allow for global convergence (see Figure 11d). **In Model Crust 2, the initial cohesion is randomly perturbed.

where $\dot{\lambda}$ is a plastic multiplier and Q is assumed to have a form similar to that of the yield function F:

$$Q = \sqrt{J_2} - P\sin(\psi), \tag{7}$$

with $\psi \leq \phi$ the dilation angle.

Next, we consider an visco-elasto-plastic model classically used in geodynamics (Figure 1b) with a viscous damper added in series to the previous rheology (Maxwell-type approach, V-E-P):

$$\dot{\epsilon} = \dot{\epsilon}^{\mathrm{v}} + \dot{\epsilon}^{\mathrm{e}} + \dot{\epsilon}^{\mathrm{p}}, \tag{8}$$

the superscript v denoting a viscous (strain) component. The viscous deviatoric strain rate $\dot{\epsilon}^{\mathrm{v}\,\prime}$ is assumed to be linearly related to the deviatoric stress tensor:

$$\dot{\epsilon}^{\mathrm{v}\,\prime} = \frac{\tau}{2\eta}, \tag{9}$$

with η the (constant) dynamic shear viscosity.

Third, we consider a model where the plastic element of Figure 1a is substituted by a viscoplastic element (Figure 1c), which can be considered as a Kelvin-type arrangement (E-VP):

$$\dot{\epsilon} = \dot{\epsilon}^{\mathrm{e}} + \dot{\epsilon}^{\mathrm{vp}}. \tag{10}$$

During viscoplastic flow, the yield function is now defined as (Heeres et al., 2002):

$$F = \sqrt{J_2} - C\cos(\phi) - P\sin(\phi) - \eta^{\mathrm{vp}}\dot{\lambda}, \tag{11}$$

where η^{vp} is the viscosity of the damper. The rate-independent limit is recovered by letting $\eta^{\mathrm{vp}} \to 0$. Expression (11) makes the yield function rate dependent, so this model belongs to the class of consistency viscoplastic models. It has been shown (Heeres et al., 2002; Wang et al., 1997) that this class of viscoplastic models has advantages over overstress-type viscoplastic models, for example, those of the Perzyna-type (Perzyna, 1966), including an improved convergence behavior and a more straightforward implementation.

3. Numerical Implementation

The expression of the viscoelastic tangent matrix $\mathbf{D}^{\mathrm{ve}}$ is obtained by integrating the Maxwell rheological chain, equation (8) under the assumption of no plastic flow. We introduce the quantities

$$G^{\mathrm{ve}} = \left(\frac{1}{G} + \frac{\Delta t}{\eta}\right)^{-1} \quad \text{and} \quad \xi = \frac{G^{\mathrm{ve}}}{G} \tag{12}$$
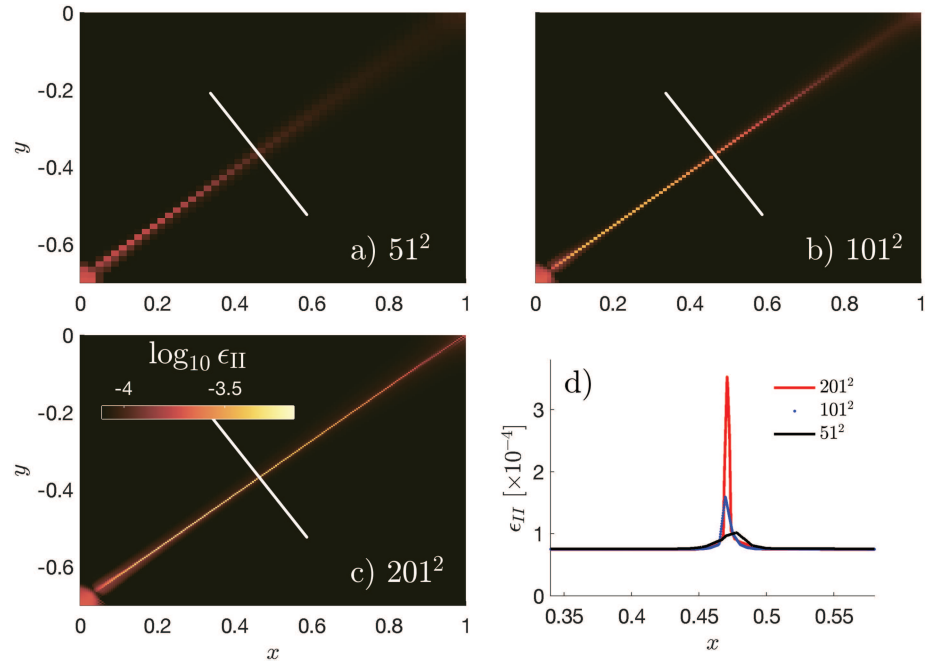
Figure 2. Spatial distribution of accumulated strain (ϵ_{II}) calculated with an elasto-plastic rheology for three different mesh resolutions: (a) 51^2, (b) 101^2, and (c) 201^2 nodes. Results are depicted after a bulk strain of $\approx 7.7 \times 10^{-5}$. The white lines indicate the location of solution profiles reported in (d). (d) Profiles of accumulated strain (a) probed across elasto-plastic shear bands.

to obtain the following update rule for the total stress tensor:

$$\boldsymbol{\sigma}^{t+1} = -\mathbf{i}P^t + \xi\boldsymbol{\tau}^t + \mathbf{D}^{\text{ve}}\left(\Delta\boldsymbol{\epsilon}^{\text{ve}}\right)^{t+1}, \tag{13}$$

where the Δ-operator represents a finite increment and $\mathbf{i} = [1, 1, 1, 0]^T$. The visco-elastic tangent operator reads:

$$\mathbf{D}^{\text{ve}} = \begin{bmatrix} K + \frac{4}{3}G^{\text{ve}} & K - \frac{2}{3}G^{\text{ve}} & K - \frac{2}{3}G^{\text{ve}} & 0 \\ K - \frac{2}{3}G^{\text{ve}} & K + \frac{4}{3}G^{\text{ve}} & K - \frac{2}{3}G^{\text{ve}} & 0 \\ K - \frac{2}{3}G^{\text{ve}} & K - \frac{2}{3}G^{\text{ve}} & K + \frac{4}{3}G^{\text{ve}} & 0 \\ 0 & 0 & 0 & G^{\text{ve}} \end{bmatrix}, \tag{14}$$

with K the elastic bulk modulus.

If (visco)plastic flow has occurred, the incremental plastic multiplier, $\Delta\lambda$, must be computed from equation (11) with $\dot{\lambda} = \frac{\Delta\lambda}{\Delta t}$ and $F = 0$; see also Heeres et al. (2002). Using a Taylor's expansion for the yield function (de Borst & Feenstra, 1990; Duretz et al., 2018), or by considering that the corrected stress state lie onto the yield surface (de Souza Neto et al., 2008), a closed-form expression for $\Delta\lambda$ can be derived for a Drucker-Prager yield function:

$$\Delta\lambda = \frac{F(\boldsymbol{\sigma}^{\text{trial}})}{G^{\text{ve}} + K\sin(\phi)\sin(\psi) + \frac{\eta^{\text{vp}}}{\Delta t} + H}, \tag{15}$$

where $\boldsymbol{\sigma}^{\text{trial}}$ is the trial stress, which has been computed assuming no (visco)plastic flow, and

$$H = h\cos\phi\sqrt{\frac{2}{3}\left(\frac{\partial Q}{\partial\boldsymbol{\sigma}}\right)^T\frac{\partial Q}{\partial\boldsymbol{\sigma}}}. \tag{16}$$

Defining $\boldsymbol{\sigma}^t$ as the stress state at the beginning of the loading step, the new stress state can be computed by adding the viscoelastic stiffness times the difference of the total and the (visco)plastic strain increments to $\boldsymbol{\sigma}^t$:

$$\boldsymbol{\sigma}^{t+1} = \boldsymbol{\sigma}^t + \mathbf{D}^{\text{ve}}(\Delta\boldsymbol{\epsilon} - \Delta\boldsymbol{\epsilon}^{\text{vp}}) = \boldsymbol{\sigma}^t + \mathbf{D}^{\text{ve}}\left(\Delta\boldsymbol{\epsilon} - \Delta\lambda\frac{\partial Q}{\partial\boldsymbol{\sigma}}\right), \tag{17}$$
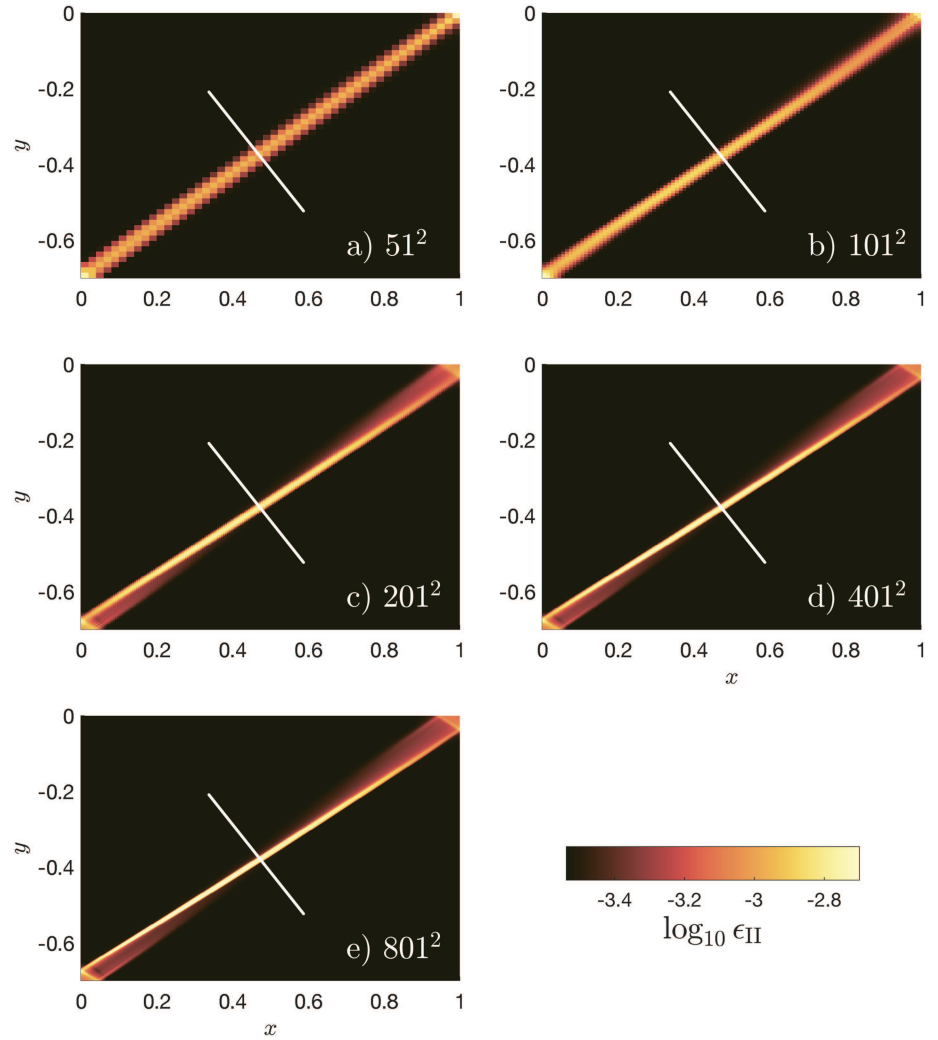
Figure 3. Spatial distribution of accumulated strain (ϵ_{II}) calculated with an elasto-viscoplastic rheology for five different mesh resolutions: (a) 51^2, (b) 101^2, (c) 201^2, (d) 401^2, and (e) 801^2 nodes. Results are depicted after a bulk strain of 3.0×10^{-4}. The white lines indicate the location of solution profiles reported in Figure 4.

which exactly satisfies the yield condition.

When a Newton-Raphson iterative procedure is used to achieve global equilibrium, the above expression must be linearized. This leads to the so-called consistent tangent operator for visco-elastic-viscoplastic solids

$$\mathbf{D}^{\text{vep}} \equiv \frac{\partial \boldsymbol{\sigma}}{\partial \boldsymbol{\epsilon}} = \mathbf{E}^{-1} \mathbf{D}^{\text{ve}} - \frac{\mathbf{E}^{-1} \mathbf{D}^{\text{ve}} \frac{\partial Q}{\partial \boldsymbol{\sigma}} \left(\frac{\partial F}{\partial \boldsymbol{\sigma}} \right)^T \mathbf{E}^{-1} \mathbf{D}^{\text{ve}}}{H + \frac{\eta^{\text{vp}}}{\Delta t} + \left(\frac{\partial F}{\partial \boldsymbol{\sigma}} \right)^T \mathbf{E}^{-1} \mathbf{D}^{\text{ve}} \frac{\partial Q}{\partial \boldsymbol{\sigma}}}, \tag{18}$$

with Δt the time step and

$$\mathbf{E} = \mathbf{I} + \Delta \lambda \frac{\partial^2 Q}{\partial \boldsymbol{\sigma}^2}. \tag{19}$$

Detailed derivations of the consistent tangent operator and incremental plastic multiplier are provided in Appendices A and B.

4. Model Configuration

The results shown in this study have been obtained using a simple initial model configuration. The two-dimensional model consists of a 1.0×0.7 domain subjected to a kinematic boundary condition, which
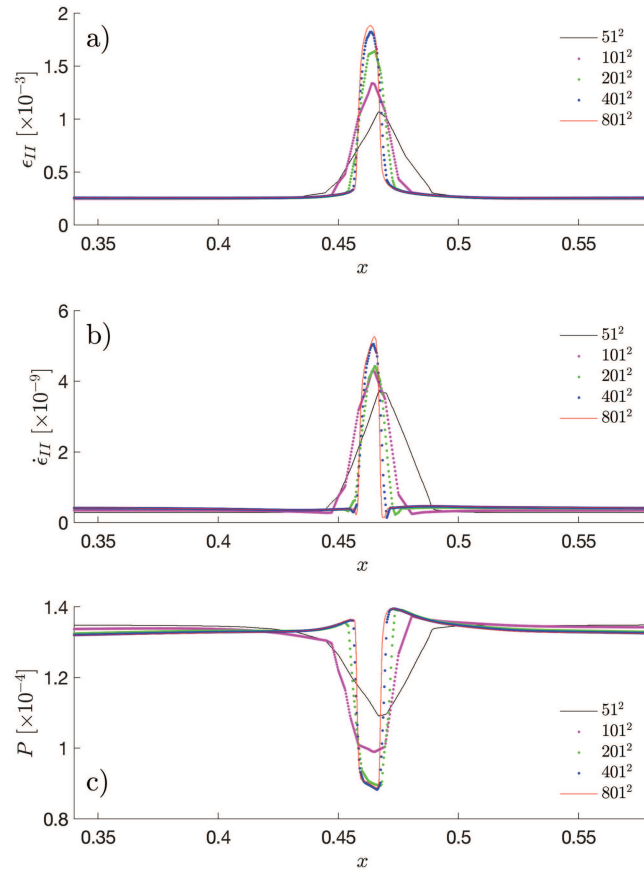
Figure 4. Profiles of (a) accumulated strain, (b) effective strain rate, and (c) pressure probed across elasto-viscoplastic shear bands. The results were obtained on five different mesh resolutions (51^2, 101^2, 201^2, 401^2, and 801^2 nodes). The solution profiles were sampled along the white lines visible on Figure 3.

induces a pure shear state. Displacements increments ($\Delta u_x^{\text{BC}} = -x\Delta\epsilon^{\text{BC}}$, $\Delta u_y^{\text{BC}} = y\Delta\epsilon^{\text{BC}}$) are imposed on the south and east sides of the domain. The west and north sides of the domain are slip-free boundaries. A circular inclusion with radius 5×10^{-2} is located at the southwest corner of the domain. This imperfection is characterized by a lower shear modulus, which causes the stress perturbation ultimately leading to strain localization. All initial stress and strain components are set equal to zero. We have used the same number of nodes (n_i) in both spatial dimensions ($n_x = n_y$). The shear modulus G has been set equal to 1 in the matrix and equal to 0.25 in the perturbation, while the bulk modulus K has been set equal to 2. The applied strain increment $\Delta\epsilon_{\text{BG}} = 5.0 \times 10^{-6}$. For the viscoplastic model, the viscosity is set to 2.5×10^2 and the time step $\Delta t = 10^4$, which yields a background strain rate $\dot{\epsilon}_{\text{BG}} = \frac{\Delta\epsilon_{\text{BG}}}{\Delta t} = 5.0 \times 10^{-9}$. More information about the model parameters is given in Table 1.

5. Modeling Results with an Elasto-Plastic Rheology (E-P Model)

The first series of computations have been carried using a rate-independent elasto-plastic rheology, an angle of internal friction $\phi = 30°$, and a dilatancy angle $\psi = 10°$. Three different resolutions were employed, with $n_i = [51, 101, 201]$ nodes. Figure 2 shows the second invariant of the accumulated strain for all three resolutions, for the same amount of applied background strain. A single shear band develops starting from the imperfection. The shear band is oriented at $35°$ from the direction of the principal compressive stress, which is in line with the Arthur formula, $45° - 1/4(\phi + \psi)$ (Arthur et al., 1977; Kaus, 2010), which has been experimentally observed for shear banding in sands and can be derived from bifurcation analysis using the Mohr-Coulomb criterion. For the Drucker-Prager yield criterion, the out-of-plane stress, however, plays a role (Rudnicki & Rice, 1975), but this apparently affects the numerical results only marginally. The results are clearly mesh dependent as the localized strain is distributed over a thickness of a single cell.
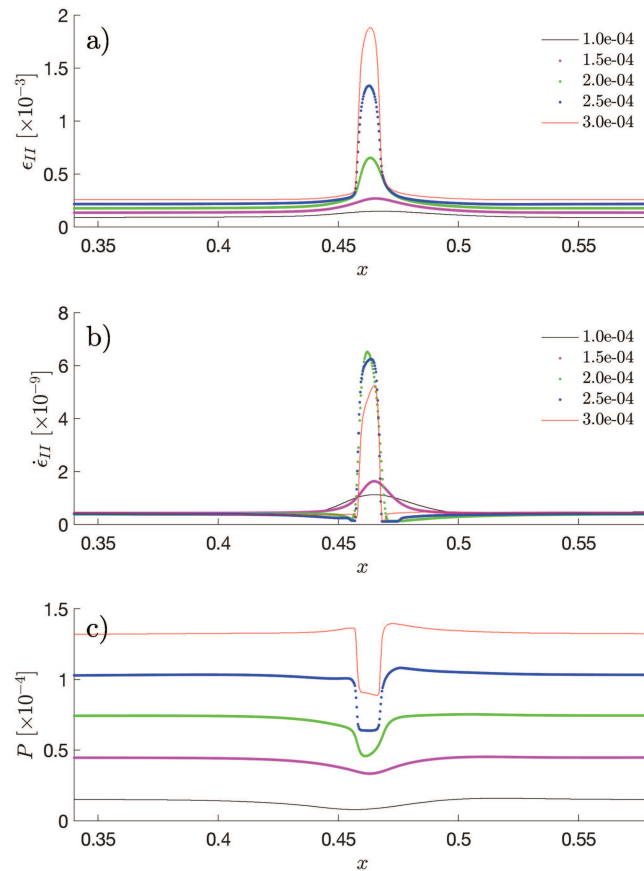
Figure 5. Temporal evolution of (a) accumulated strain, (b) effective strain rate, and (c) pressure across the shear zone. The different profiles correspond to five values of background strain (from 1.0×10^{-4} to 3.0×10^{-4}). Results were computed on a mesh consisting of 401^2 nodes.

Another representation was made by plotting the profiles of the second invariant of the accumulated strain invariant and of the pressure across the shear bands (see Figure 2d). The profiles reveal a divergence of the solutions with increasing resolution. Since the displacement jump across the shear band is constant, the magnitude of strain in the shear band continues to increase for finer resolutions. For the finest discretization, we observe the development of a Dirac-like strain distribution. This is further evidence for the ill-posed character of the boundary value problem, since the Dirac-like strain profile points at a discontinuity in the displacements, which can only occur if the governing equations have locally changed character from elliptic to hyperbolic.

6. Results for An Elasto-Viscoplastic Rheology (E-VP Model)

The second series of models were carried out using a elasto-viscoplastic rheology. The numerical simulations were achieved on progressively refined meshes consisting of $n_i = [51, 101, 201, 401, 801]$ nodes. Figure 3 depicts the spatial distribution of the accumulated strain at a fixed amount of shortening (3.0×10^{-4}). In contrast with the elasto-plastic models of Figure 2, shear bands of a finite width now arise. We note that the shear band is still oriented at 35° from the direction of σ_1. Detailed probing of different variables, in particular the pressure, the second invariant of the accumulated strain and strain rate, results in a clear convergence upon mesh refinement (see Figure 4). The strain and strain rate profiles across the shear bands have a quasi–Gaussian shape. The peak strain and the peak strain rate are at the center of the shear band and reach values of 1.8×10^{-3} and 5.3×10^{-9}, respectively. The pressure is lower inside the shear band and reaches a minimum value of 0.9×10^{-4}. For a low resolution (51^2 nodes), the peak strain reaches about half the magnitude of that obtained with the higher resolutions and the strain is localized over a wider zone.

The evolution of the strain, the strain rate, and the pressure across the shear band is shown in Figure 5a for a given fixed resolution. From a background strain of 1.0×10^{-4}, the strain locally increases inside a
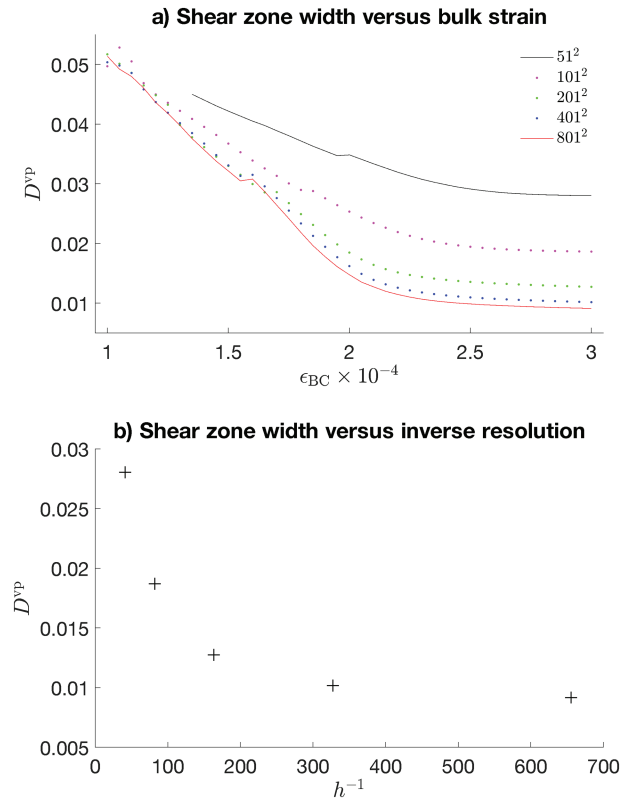
a) Shear zone width versus bulk strain

b) Shear zone width versus inverse resolution

Figure 6. (a) Evolution of the characteristic shear zone thickness (D^{vp}) versus accumulated background strain (ϵ_{BG}). The values were extracted from the runs with five different mesh resolutions (Figure 3). (b) Characteristic shear band thickness (D^{vp}) versus grid spacing h. The results were extracted from the runs depicted on Figure 3.

well-defined region. The amplitude of a Gaussian-like strain profile exhibits a growth of 1.8×10^{-3} over an increment of background strain of 2.0×10^{-4} (see Figure 5a). The evolution of the second invariant of the strain rate shares these characteristics. The amplitude of the Gaussian-like profile of the strain rate reaches a peak value of 6.2×10^{-9} shortly after the onset of shear localization (background strain 2.0×10^{-4}). This corresponds to a magnitude of the strain rate that is approximately 12 times larger than the applied background strain rate. The profiles of the pressure are characterized by a progressive decrease towards the center of the shear zone. After an applied background strain of 3.0×10^{-4}, the pressure in the shear band drops to about two thirds the background pressure. The shape of the pressure profile differs from that of the accumulated strain rate profiles. With ongoing strain, it progressively deviates from a Gaussian shape and morphs into a square shape. At the final stage, positive pressures develop adjacent to the shear zone, which further increases the magnitude of the pressure gradient across the shear band.

7. Characteristic Shear Bandwidth

The above results indicate that the viscoplastic rheology introduces a length scale into the boundary value problem. In the following, we define the characteristic shear-band thickness (D^{vp}) as the bandwidth of the accumulated strain profiles, which can be extracted from the two-dimensional modeling. Since the strain rate profiles sampled normal to the shear band exhibit a Gaussian-like shape, they can approximated as

$$\dot{\epsilon} = \dot{\epsilon}^{max} \exp\left(-\frac{z^2}{D^{vp^2}}\right),\tag{20}$$

where z is coordinate orthogonal to the shear band and $\dot{\epsilon}^{max}$ is the maximum value of second strain rate invariant along the profile. The value of D^{vp} is obtained by an optimum fit of the Gaussian equation to the profiles that have been extracted from the two-dimensional models.
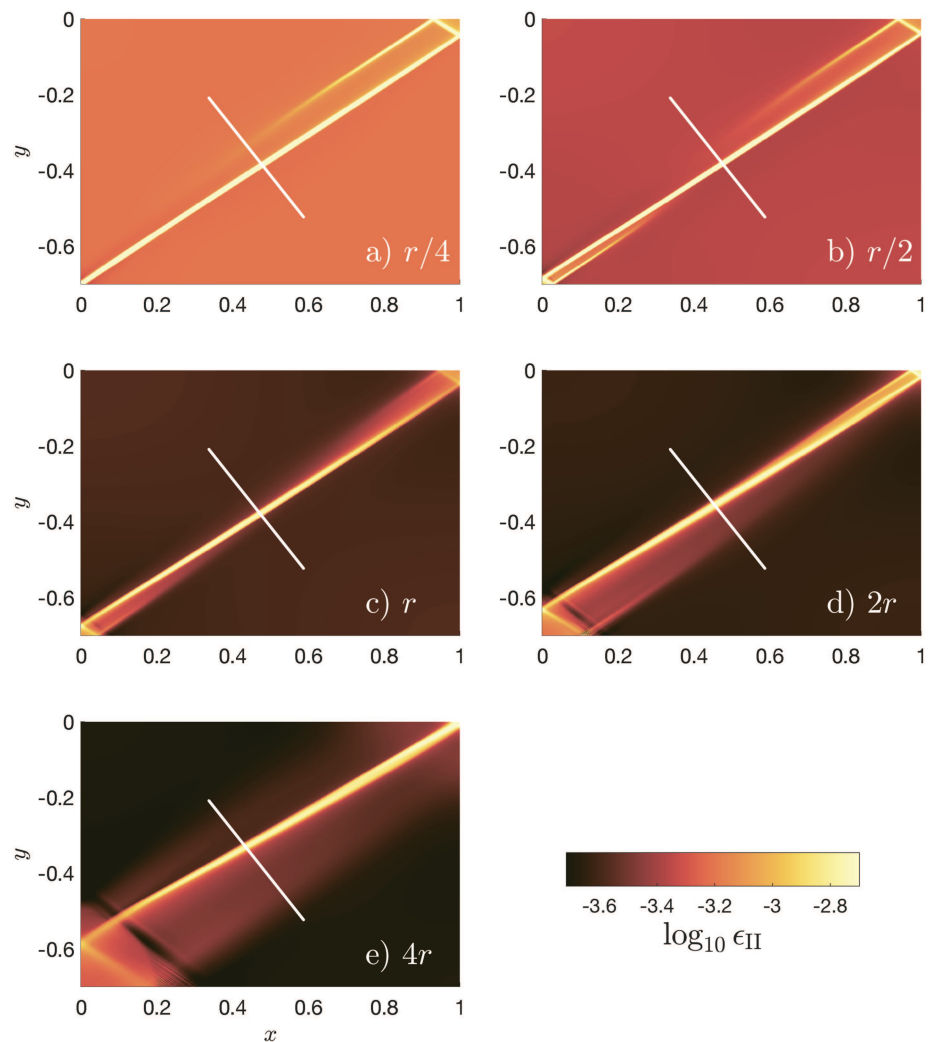
Figure 7. Influence of the initial size of the imperfection on the shear bands. Models were run with five different initial seed radius and for a fixed resolution of 401^2 nodes. The radius of the imperfection in the reference model is r (panel c). The inclusion has a reduced size in panels (a) and (b) and an increased size in panels d) and e). No material softening was applied.

The transient evolution D^{vp} for different mesh resolutions is given in Figure 6a. For all resolutions, the initial value of D^{vp} is equal to the radius of the initial perturbation ($r = 0.05$). The values of D^{vp} progressively decrease with an increasing applied strain. They all reach an asymptotic value at an applied strain of approximately 2.5×10^{-4}. We have plotted the asymptotic D^{vp} values as a function of the grid spacing h^{-1} in Figure 6b. The shear bandwidth asymptotically approaches a value of 0.01 with an increasing resolution.

Using a similar rheological model, Wang et al. (1996) have quantified the impact of the dimension of the initial imperfection on the shear bandwidth. The dimensions of the initial perturbation are, together with the material parameters, key to the occurrence and further evolution of shear localization. It plays a fundamental role at the onset of shear localization. However, when the shear zone reaches a steady-state situation, that is, when the width D^{vp} has stabilized, the shear bandwidths are virtually independent of the size of the imperfection, as shown in Figure 7. This is similar to results obtained with thermo-mechanical models of strain localization in temperature activated rate-dependent materials (Lemonds & Needleman, 1986) using a power law viscous rheology (Duretz et al., 2014) and a power law viscoelastic rheology (Duretz et al., 2015). In a steady state, the characteristic shear-band thickness is essentially independent of the size of the imperfection.
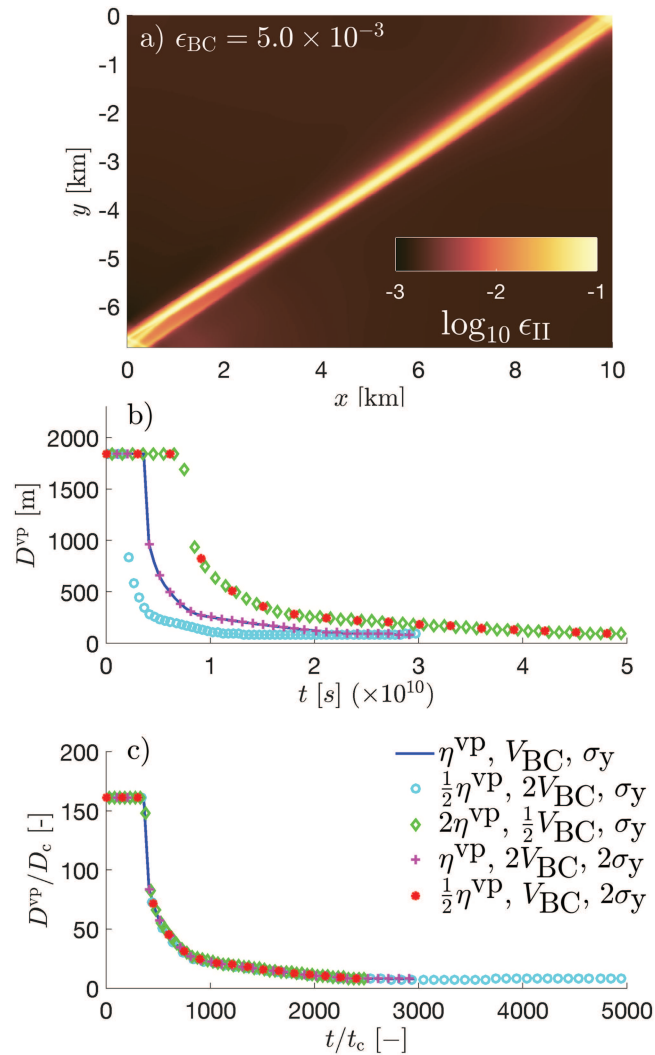
Figure 8. Strain localization at the kilometer scale arising from a single material perturbation. Panel (a) depicts the strain field after a bulk strain of 5×10^{-3}. Panel (b) shows measured shear bandwidths for different parameter combinations. Panel (c) depicts the master curve obtained when defining the characteristic time directly proportional to the Kelvin element viscosity.

8. Modeling Strain Localization at the Crustal Scale

In order to investigate the applicability and consequences of viscoplasticity for modeling lithospheric deformations, we have carried out simulations on kilometer-scale dimensions, using typical material parameters for rocks (*Model Crust 1* and *Model Crust 2*; see Table 1). *Model Crust 1* was designed to study the initiation and propagation of a single shear band, which originates from a well-defined material imperfection using cohesion softening. The configuration shares similarities with that of *Model E-VP* but has a material imperfection with radius of 500 m. The shear modulus within the perturbation is equal to 25% of that in the matrix (Table 1). The boundary velocity was set to $V_{BC} = 2 \times 10^{-9}$ m/s. The dimensions of the domain are 10×6.85 km, which is discretized using 400^2 cells leading to a resolution of 25 m. For the reference test, the Kelvin element viscosity was set to 10^{17} Pa · s, and the initial cohesion was set to $C = 1.75 \times 10^7$ Pa. Softening was prescribed by setting a negative value of hardening modulus, $h = -7.0 \times 10^7$ Pa, and allowing a reduction of cohesion by a factor 2. The shear band develops from the southwest corner towards the northeast corner (see Figure 8a). As for the previous cases, strain localization is progressive, and the shear bandwidth narrows down with increasing time or strain (Figure 8b) and progressively reaches a width of 90 m. In order to test the sensitivity of the model, we have tested different parameter combinations, all satisfying a constant value the product $\frac{\eta^{vp} V_{BC}}{C}$. The resulting models all predict a final shear band thickness of
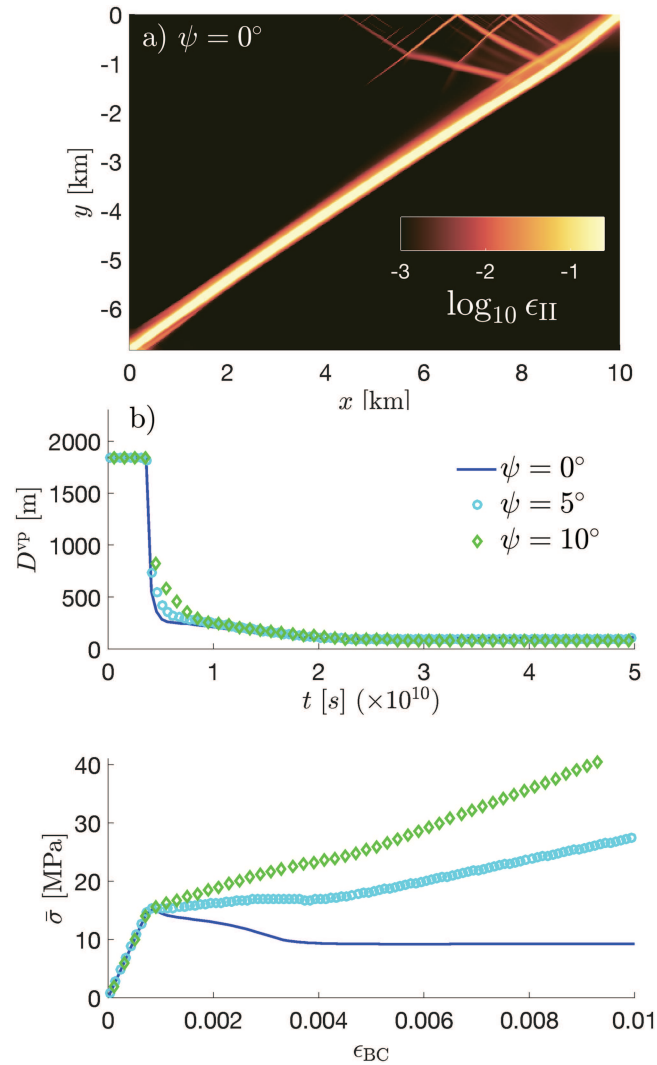
Figure 9. Effect of plastic dilatancy on shear band development. Panel (a) depicts the strain field after a bulk strain of 1×10^{-2} in the incompressible limit ($\psi = 0°$). Panel (b) shows measured shear bandwidths for different values of dilatancy angle. Panel (c) depicts stress-strain curves for the different values of ψ.

about 90 m. The time needed for strain localization is proportional to the Kelvin element viscosity. Defining the characteristic time $t_c \propto \frac{\eta^{vp}}{G}$ and the characteristic length $D_c \propto \frac{\eta^{vp} V_{BC}}{C}$ allows to collapse the shear-band thickness evolution onto a single master curve (Figure 8c).

When considering crustal-scale strain localization, incompressible plastic deformation is generally invoked. However, with rate-independent plastic models, such a limit poses serious numerical issues. The latter occur for large differences between the friction and dilation angles ($\phi - \psi > 20°$) and are caused by the loss of ellipticity (Sabet & de Borst, 2019). In practice, models often diverge (e.g., Spiegelman et al., 2016) even when using consistent linearizations (e.g., Duretz et al., 2018). With Kelvin-type viscoplasticity models, attainment of convergence appears to be much less problematic because of the weak regularization of the ill-posed problem. Fully converged results were obtained for $\psi = 0°$ and $\phi = 30°$ as depicted on Figure 9a. Interestingly, strain localization was obtained for values of the dilation angle up to 10°, but localization did not occur for larger values of ψ. During localization, the shear zone narrows down at a faster rate when the dilation angle is small (Figure 9b). However, the width of the postlocalization shear zone is not affected by a variations of ψ (Figure 9b). By contrast, stress-strain curves notably differ for the different values of ϕ. In the incompressible limit, the effective stress ($\bar{\sigma} = \frac{1}{V} \int \sqrt{J_{II}} dV$) reaches a peak value (15 MPa) and then decreases to a
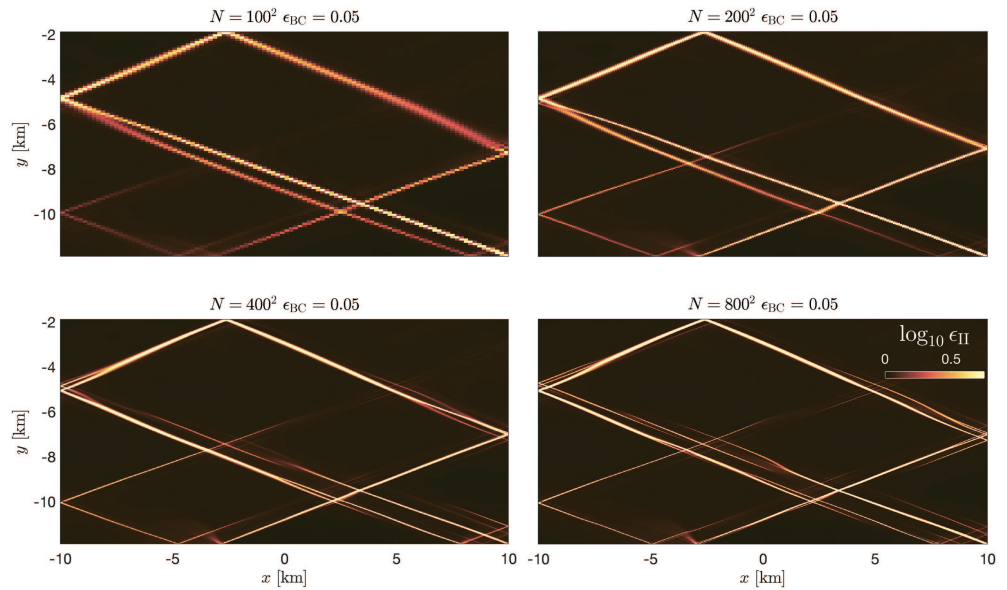
Figure 10. Shear banding at kilometer scale arising from an initial random perturbation of the initial cohesion field for various mesh resolutions (from 100^2 to 800^2 cells). A Kelvin E-VP rheological model was applied. The confining pressure was set to 50 MPa, and the Kelvin element viscosity was set to $\eta^{VP} = 3 \times 10^{18}$ Pa·s.

saturation value (≈ 10 MPa). For larger angles, the effective stress keeps increasing despite the occurrence of strain localization.

In *Model Crust 2*, strain localization is seeded by setting an initial random perturbation on the cohesion field. The confinement pressure was set equal to 50 MPa, and cohesion softening is again applied. Numerous intersecting shear bands develop (see Figure 10). Due to the complex internal kinematics, shear bands exhibit different lengths and widths. This is in contrast with previously presented models in which single shear bands were arising from single perturbations (Figure 8a). We have run simulations for various resolutions ($n_i = [101, 201, 401, 801]$) up to a bulk strain of 0.5×10^{-2}. The results show that, despite the use of nonassociated plasticity and cohesion softening, a reasonable convergence upon mesh refinement was achieved. While there is a difference in the strain fields between the low-resolution models, for example, between 100^2 and 200^2 cells, the differences are much less pronounced when comparing simulations for higher resolutions, for example, between 400^2 and 800^2 cells. Most importantly, global equilibrium iterations converged quadratically up to machine precision without any need to reduce the applied strain increment. This is in complete contrast with rate-independent elasto-plastic models, with which it was impossible to reach such a high accuracy (results not shown here).

9. Discussion

9.1. A Potential Regularization for Mesh-Dependent Strain Softening Plasticity

In tectonic modeling, strain localization in the frictional domain is generally modeled using a strain-softening parametrization, for example, Huismans and Beaumont (2002). A progressive decrease of the magnitude of plastic parameters (cohesion, friction angle) is imposed as a function of the accumulated plastic strain. Such a parametrization is supposed to mimic the effects of complex physicochemical processes (e.g., metamorphic reactions and fluid pressure variations) that are not taken into account in the model description, which may cause postlocalization stress drops measured in experiments on rock deformation. However, this approach is known to suffer from mesh dependence. Among the numerous possibilities that provide regularization of mesh dependence in plasticity, viscoplasticity is a simple and efficient solution. Herein, we have shown that using a viscoplastic rheology together with a nonassociated frictional plasticity model and cohesion softening provides results that converge upon mesh refinement. Morerover, we have found that viscoplasticity also facilitates resolving strain localization in the incompressible plastic limit ($\psi = 0$), which is very relevant for lithospheric conditions.

Table 2
Number of Newton-Raphson Iterations Required to Reach Global Equilibrium for Different Resolutions Using Either the E-P or the E-VP Model

E-P models	51^2	101^2	201^2	401^2
Mean # its.	3.88	6.78	– – –	– – –
Max. # its.	11	26	– – –	– – –
E-VP models	51^2	101^2	201^2	401^2
Mean # its.	3.88	4.17	4.41	4.89
Max. # its.	11	12	12	12

Note. The relative tolerance was set to 10^{-11} and was measured using the L_2 norm. Runs that did not result in a converged state are denoted by a dash.

9.2. Benefits for the Convergence Behavior of the Global Nonlinear Solver

The use of a viscoplastic model as regularization method can also dramatically improve global convergence and the computability and solvability of shear banding. With a viscoplastic model, strains are not concentrated in one cell but are distributed over a finite width. Therefore, increasing the resolution does not lead to an increase of the strain locally, which can cause serious numerical issues such as local snapbacks in the return mapping and the occurrence of multiple, nonphysical equilibrium states that cause divergence of the global equilibrium-finding iterative procedure. An illustration is that for an elasto-plastic rheology, no results could be obtained for meshes with more than 201^2 nodes, even when reducing the strain increment. When the strain increment was kept constant, it was not possible to reach convergence for resolutions with more than 101^2 nodes (Table 2). Using an elasto-viscoplastic rheology, however, converged results were obtained for fine resolutions, up to 801^2 nodes (Figures 3 and 10). Moreover, both the maximum and average number of iterations required to achieve global equilibrium are almost insensitive to the numerical resolution, as expected (Table 2).

9.3. Implications of Viscoplasticity

The viscoplastic model introduces a rate dependence in the yield function and requires an additional model parameter: the viscosity of the viscoplastic (Kelvin) element. Here, we used the viscosity as a numerical parameter rather than as an experimentally measured quantity with a clear physical meaning. Shear viscosities estimated from laboratory experiments of rock deformation exhibit an Arrhenius temperature dependence, which results in a exponential growth of viscosity with decreasing temperature. Using such values as viscosity of the Kelvin element would lead to an unrealistic overshoot of the yield function in the frictional (low temperature) domains of the lithosphere and would preclude strain localization. We believe that the viscosity of the Kelvin element should be chosen such that shear bands can be resolved numerically. We expect that such an approach will allow for the converged resolution of shear bands in geodynamic models where the spatial resolution has so far at most reached the 100-m scale. Another approach to select the Kelvin element viscosity is to reason in terms of the overstress ($\bar{\sigma} = \eta^{\mathrm{vp}} \dot{\lambda}$). By assuming that the rate of the plastic multiplier is proportional to the background strain rate ($\dot{\lambda} \propto LV_{\mathrm{BC}}$), it is possible to define the viscosity that will approximately generate the predefined overstress ($\eta^{\mathrm{vp}} \propto \frac{\bar{\sigma}}{LV_{\mathrm{BC}}}$). For example, using the parameters of *Model Crust 1* (Figure 8) and assuming an overstress of 20 kPa, one obtains a viscosity for the Kelvin element of 10^{17} Pa·s.

In general, the width of shear bands that arise in the frictional domains of the lithosphere is highly variable and can range from discrete fault planes to finite thickness fault zones (gouges), which involve complex processes that are beyond the scope of this study (shear heating, fluid pressure variations, grain crushing, and mineral reactions). A detailed study of these processes may provide a physics-based regularization for the width of frictional shear bands, which will likely be smaller than the current resolution power of geodynamic models.

9.4. Differences with the Standard Visco-Elasto-Plastic Model

In geodynamics, visco-elasto-plasticity is generally implemented via a rheological model, which couples a viscous damper, an elastic spring, and a plastic slider in series, which can be dubbed a Maxwell V-E-P model, for example, Lemiale et al. (2008), Gerya and Yuen (2007), and Kaus (2010). With such a model,
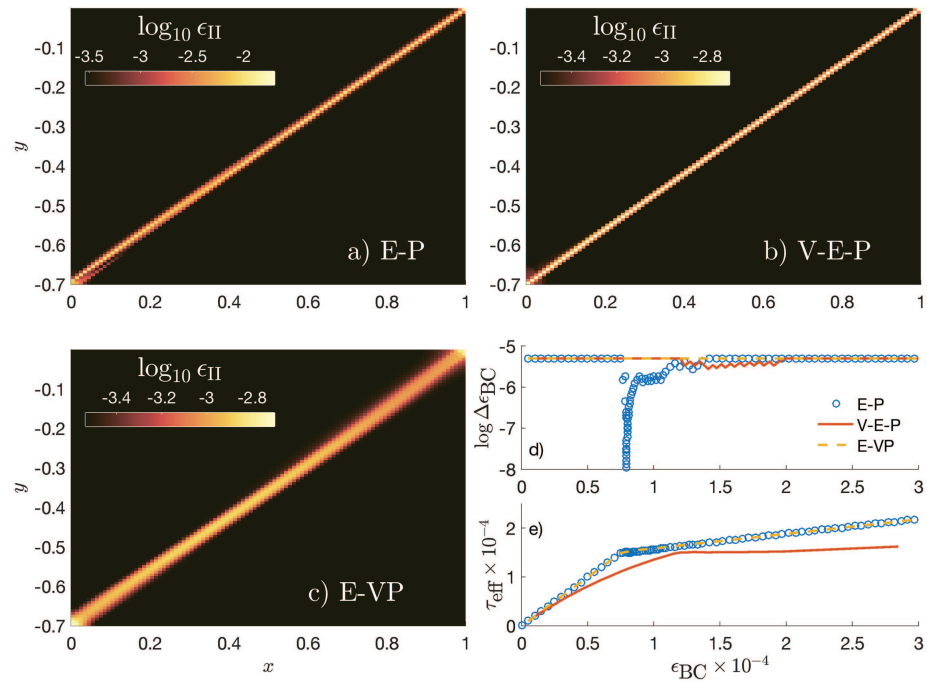
Figure 11. Spatial distribution of accumulated strain (ϵ_{II}) after a bulk strain of 3.0×10^{-4}. Panel (a) depicts the results obtained with an elasto-plastic rheology (E-P). Panel (b) corresponds to a visco-elasto-plastic rheology (V-E-P) using a serial viscosity of 2.5×10^5. Panel (c) shows the results obtained with an elasto-viscoplastic rheology (E-VP) using a Kelvin viscosity of 2.5×10^2. Panel (d) shows the variations of the strain increment needed for achieving successful nonlinear solutions. Panel (e) shows the evolution of effective stress for the three different rheological models.

rate dependence is included in the visco-elastic trial stress but not in the plastic strain component. Shear localization obtained with such models has the same characteristics as that obtained with a rate-independent elasto-plastic rheology. Shear bands localize on a single band of cells or elements, thus causing numerical simulations to be mesh sensitive (see Figures 11a and 11b). This is in contrast with the model discussed above, which incorporates rate dependence in the plastic element and allows shear localization to spread over several cells or elements (see Figure 11c).

Simulations with an elasto-plastic model may also require extremely fine load increment to reach global equilibrium, as shown in Figure 11d. This equally applies to models with a viscoelastic-plastic (V-E-P) rheology. Elasto-viscoplastic (E-VP) models overcome this issue (Figure 11d) and can accurately compute the load-bearing capacity of an E-P material (see Figure 11e).

For geodynamics modeling purposes, we suggest that E-VP and V-E-P models could be combined into an E-V-VP model, shown in Figure 1d. On the one hand, Maxwell visco-elasticity is necessary to capture both the short timescale (Deng et al., 1998; Heimpel, 2006; Wang, 2007) and the long timescale, for example, Farrington et al. (2014), Schmalholz et al. (2015), and Olive et al. (2016), which are essential features of lithospheric deformations. On the other hand, Kelvin-type viscoplastic models remedy known issues in modeling strain localization in the lithosphere. A combined E-V-VP model would be suitable to capture the visco-elastic behavior of rocks but would also enable to obtain mesh-independent and globally convergent solutions of plastic shear banding.

10. Conclusions

We have investigated the role of elasto-viscoplasticity with a damper in parallel to a plastic slider (Kelvin-type rheology) on the development of shear bands in the frictional regions of the lithosphere. While the rate-independent frictional plasticity models, which have been used classically, suffer from mesh sensitivity, models using this viscoplastic rheology converge upon mesh refinement. The strain, the strain rate, and the pressure inside the shear bands reach finite values upon a decrease of the grid spacing. A characteristic length scale is introduced due to the rate dependence of the viscoplastic model. Our results indicate that

shear bands that arise from pressure-dependent viscoplasticity maintain their orientation but are now also equipped with a characteristic bandwidth. Even the combination of a Kelvin-type viscoplasticity with strain softening on the cohesion gives a mesh-convergent behavior. The approach is thus a viable way to regularize strain localization in geodynamic models. Most importantly, the introduction of an internal length scale due to viscoplasticity maintains well posedness of the boundary value problem also during shear banding, and therefore markedly improves the convergence of equilibrium iterations, which is a recurrent issue in geodynamic simulations.

Appendix A: The Incremental Plastic Multiplier

For (visco)plastic deformations to occur, the stress must lie on the yield surface and continue to be on the yield surface for an infinitesimal time increment when adopting the consistency model of viscoplasticity (Heeres et al., 2002; Wang et al., 1997). This implies that for the yield function at the end of the plastic increment, we must have $F^{t+1} = 0$. Following de Souza Neto et al. (2008), the corrected total stress is given by

$$\sigma^{t+1} = \left(1 - \frac{G^{ve}\Delta\lambda}{\sqrt{J_{II}^{trial}}}\right)\sigma^{trial}. \tag{A1}$$

Using the identity $\frac{\sigma^{t+1}}{\sqrt{J_{II}^{t+1}}} = \frac{\sigma^{trial}}{\sqrt{J_{II}^{trial}}}$, the corrected second stress invariant is

$$\sqrt{J_{II}^{t+1}} = \sqrt{J_{II}^{trial}} - G^{ve}\Delta\lambda. \tag{A2}$$

The corrected pressure reads

$$P^{t+1} = P^{trial} + K\sin(\psi)\Delta\lambda, \tag{A3}$$

and the updated cohesion can be expressed as

$$C^{t+1} = C^{trial} + H\Delta\lambda. \tag{A4}$$

Approximating the rate of the plastic multiplier as $\dot{\lambda} = \frac{\Delta\lambda}{\Delta t}$, the yield function at the end of the plastic increment can be written explicitly as

$$F^{t+1} = \sqrt{J_{II}^{trial}} - G^{ve}\Delta\lambda - \cos(\phi)\left(C^{trial} + H\Delta\lambda\right) - \sin(\phi)\left(P^{trial} + K\sin(\psi)\Delta\lambda\right) - \eta^{vp}\frac{\Delta\lambda}{\Delta t}. \tag{A5}$$

Solving for $F^{t+1} = 0$ then yields the following expression for the incremental plastic multiplier

$$\Delta\lambda = \frac{F^{trial}}{G^{ve} + K\sin(\phi)\sin(\psi) + \frac{\eta^{vp}}{\Delta t} + H}, \tag{A6}$$

where $F^{trial} = \sqrt{J_{II}^{trial}} - \sin(\phi)P^{trial} - \cos(\phi)C^{trial}$.

Appendix B: The Visco-Elastic-Plastic Consistent Tangent Operator

During visco-elasto-(visco)plastic straining, the stress update follows

$$\sigma^{t+1} = -P^t\mathbf{i} + \xi\tau^t + \mathbf{D}^{ve}\Delta\epsilon - \Delta\lambda\mathbf{D}^{ve}\frac{\partial Q}{\partial\sigma}. \tag{B1}$$

A small variation δ of the updated stress σ^{t+1} is given by

$$\delta\sigma = \mathbf{D}^{ve}\delta\epsilon - \delta\lambda\mathbf{D}^{ve}\frac{\partial Q}{\partial\sigma} - \Delta\lambda\mathbf{D}^{ve}\frac{\partial^2 Q}{\partial\sigma^2}\delta\sigma \tag{B2}$$

and can be recast as

$$\delta\boldsymbol{\sigma} = \mathbf{E}^{-1}\mathbf{D}^{\text{ve}}\delta\boldsymbol{\epsilon} - \mathbf{E}^{-1}\mathbf{D}^{\text{ve}}\frac{\partial Q}{\partial\boldsymbol{\sigma}}\delta\lambda \tag{B3}$$

with

$$\mathbf{E} = \mathbf{I} + \Delta\lambda\mathbf{D}\frac{\partial^2 Q}{\partial\boldsymbol{\sigma}^2}. \tag{B4}$$

We now invoke the consistency condition

$$\delta F = 0, \tag{B5}$$

which, using $F = F(\boldsymbol{\sigma}, \lambda, \dot{\lambda})$, can be elaborated as

$$\left(\frac{\partial F}{\partial\boldsymbol{\sigma}}\right)^T\delta\boldsymbol{\sigma} + \frac{\partial F}{\partial\lambda}\delta\lambda + \frac{\partial F}{\partial\dot{\lambda}}\delta\dot{\lambda} = 0. \tag{B6}$$

Premultiplying equation (B3) by $\left(\frac{\partial F}{\partial\boldsymbol{\sigma}}\right)^T$, using the approximation $\delta\dot{\lambda} = \frac{\delta\lambda}{\Delta t}$ and invoking condition (B6), provides an expression for the variation of the plastic multiplier

$$\delta\lambda = \frac{\left(\frac{\partial F}{\partial\boldsymbol{\sigma}}\right)^T\mathbf{E}^{-1}\mathbf{D}^{ve}}{H + \frac{\eta^{\text{vp}}}{\Delta t} + \left(\frac{\partial F}{\partial\boldsymbol{\sigma}}\right)^T\mathbf{E}^{-1}\mathbf{D}^{\text{ve}}\frac{\partial Q}{\partial\boldsymbol{\sigma}}}\delta\boldsymbol{\epsilon}, \tag{B7}$$

with $H \equiv \frac{\partial F}{\partial\lambda}$ and $\eta^{vp} \equiv \frac{\partial F}{\partial\dot{\lambda}}$. This expression is now substituted into equation (B3), which leads to

$$\delta\boldsymbol{\sigma} = \left(\mathbf{E}^{-1}\mathbf{D}^{\text{ve}} - \frac{\mathbf{E}^{-1}\mathbf{D}^{\text{ve}}\frac{\partial Q}{\partial\boldsymbol{\sigma}}\left(\frac{\partial F}{\partial\boldsymbol{\sigma}}\right)^T\mathbf{E}^{-1}\mathbf{D}^{\text{ve}}}{H + \frac{\eta^{\text{vp}}}{\Delta t} + \left(\frac{\partial F}{\partial\boldsymbol{\sigma}}\right)^T\mathbf{E}^{-1}\mathbf{D}^{\text{ve}}\frac{\partial Q}{\partial\boldsymbol{\sigma}}}\right)\delta\boldsymbol{\epsilon}. \tag{B8}$$

The consistent tangent operator hence reads

$$\mathbf{D}^{\text{vep}} \equiv \frac{\partial\boldsymbol{\sigma}}{\partial\boldsymbol{\epsilon}} = \mathbf{E}^{-1}\mathbf{D}^{\text{ve}} - \frac{\mathbf{E}^{-1}\mathbf{D}^{\text{ve}}\frac{\partial Q}{\partial\boldsymbol{\sigma}}\left(\frac{\partial F}{\partial\boldsymbol{\sigma}}\right)^T\mathbf{E}^{-1}\mathbf{D}^{\text{ve}}}{H + \frac{\eta^{\text{vp}}}{\Delta t} + \left(\frac{\partial F}{\partial\boldsymbol{\sigma}}\right)^T\mathbf{E}^{-1}\mathbf{D}^{\text{ve}}\frac{\partial Q}{\partial\boldsymbol{\sigma}}}. \tag{B9}$$

References

Arthur, J. R. F., Dunstan, T., Al-Ani, Q. A. J. L., & Assadi, A. (1977). Plastic deformation and failure in granular media. *Géotechnique*, *27*, 53–74.

Bažant, Z. P., & Jirasek, M. (2002). Nonlocal integral formulations of plasticity and damage: Survey of progress. *Journal of Engineering Mechanics*, *128*, 1119–1149.

Bercovici, D., Ricard, Y., & Schubert, G. (2001). A two-phase model for compaction and damage: 1. General theory. *Journal of Geophysical Research*, *106*, 8887–8906.

Buck, W. R., & Lavier, L. L. (2001). A tale of two kinds of normal fault: The importance of strain weakening in fault development. *Geological Society, London, Special Publications*, *187*, 289–303.

Buiter, S. J. H., Babeyko, A. Y., Ellis, S., Gerya, T. V., Kaus, B. J. P., Kellner, A., et al. (2006). The numerical sandbox: Comparison of model results for a shortening and an extension experiment. *Geological Society, London, Special Publications*, *253*, 29–64.

Byerlee, J. (1978). Friction of rocks. *Pure and Applied Geophysics*, *116*, 615–626.

de Borst, R. (1988). Bifurcations in finite element models with a non-associated flow law. *International Journal for Numerical and Analytical Methods in Geomechanics*, *12*, 99–116.

de Borst, R., Crisfield, M. A., Remmers, J. J. C., & Verhoosel, C. V. (2012). *Non-linear finite element analysis of solids and structures* (2nd ed.). Chichester: Wiley.

de Borst, R., & Feenstra, P. H. (1990). Studies in anisotropic plasticity with reference to the Hill criterion. *International Journal for Numerical Methods in Engineering*, *29*, 315–336.

de Borst, R., & Mühlhaus, H. B. (1992). Gradient-dependent plasticity: Formulation and algorithmic aspects. *International Journal for Numerical Methods in Engineering*, *35*, 521–539.

de Borst, R., Sluys, L. J., Mühlhaus, H.-B., & Pamin, J. (1993). Fundamental issues in finite element analysis of localisation of deformation. *Engineering Computations*, *10*, 99–122.

de Souza Neto, E. A., Perić, A., & Owens, D. R. J. (2008). *Computational methods for plasticity: Theory and applications* (1st ed.). Chichester: Wiley.

Deng, J., Gurnis, M., Kanamori, H., & Hauksson, E. (1998). Viscoelastic flow in the lower crust after the 1992 Landers, California, earthquake. *Science*, *282*, 1689–1692.

Dias da Silva, V. (2004). A simple model for viscous regularization of elasto-plastic constitutive laws with softening. *Communications in Numerical Methods in Engineering*, *20*(7), 547–568. https://doi.org/10.1002/cnm.700

Döhmann, M. J. E. A., Brune, S., Nardini, L., Rybacki, E., & Dresen, G. (2019). Strain localization and weakening processes in viscously deforming rocks: Numerical modeling based on laboratory torsion experiments. *Journal of Geophysical Research: Solid Earth*, *124*, 1120–1137. https://doi.org/10.1029/2018JB016917

Duretz, T., & Schmalholz, S. M. (2015). From symmetric necking to localized asymmetric shearing: The role of mechanical layering. *Geology*, *43*, 711–714.

Duretz, T., Schmalholz, S., & Podladchikov, Y. (2015). Shear heating-induced strain localization across the scales. *Philosophical Magazine*, *95*(28-30), 3192–3207.

Duretz, T., Schmalholz, S., Podladchikov, Y., & Yuen, D. (2014). Physics-controlled thickness of shear zones caused by viscous heating: Implications for crustal shear localization. *Geophysical Research Letters*, *41*, 4904–4911. https://doi.org/10.1002/2014GL060438

Duretz, T., Souche, A., de Borst, R., & Le Pourhiet, L. (2018). The benefits of using a consistent tangent operator for visco computations in geodynamics. *Geochemistry, Geophysics, Geosystems*, *19*, 4904–4924. https://doi.org/10.1029/2018GC007877

Farrington, R. J., Moresi, L., & Capitanio, F. A. (2014). The role of viscoelasticity in subducting plates. *Geochemistry, Geophysics, Geosystems*, *15*, 4291–4304. https://doi.org/10.1002/2014GC005507

Fullsack, P. (1995). An arbitrary Lagrangian-Eulerian formulation for creeping flows and its application in tectonic models. *Geophysical Journal International*, *120*(1), 1–23.

Gerbault, M., Poliakov, A. N. B., & Daignieres, M. (1998). Prediction of faulting from the theories of elasticity and plasticity: What are the limits? *Journal of Structural Geology*, *20*(2), 301–320.

Gerya, T. V., & Yuen, D. A. (2003). Characteristics-based marker-in-cell method with conservative finite-differences schemes for modeling geological flows with strongly variable transport properties. *Physics of the Earth and Planetary Interiors*, *140*, 293–318.

Gerya, T. V., & Yuen, D. A. (2007). Robust characteristics method for modelling multiphase visco-elasto-plastic thermo-mechanical problems. *Physics of the Earth and Planetary Interiors*, *163*, 83–105.

Hansen, D. L. (2003). A meshless formulation for geodynamic modeling. *Journal of Geophysical Research*, *108*(B11), 2549. https://doi.org/10.1029/2003JB002460

Heeres, O. M., Suiker, A. S. J., & de Borst, R. (2002). A comparison between the Perzyna viscoplastic model and the consistency viscoplastic model. *European Journal of Mechanics: A/Solids*, *21*, 1–12.

Heimpel, M. (2006). Earthquake scaling: The effect of a viscoelastic asthenosphere. *Geophysical Journal International*, *166*, 170–178.

Huismans, R. S., & Beaumont, C. (2002). Asymmetric lithospheric extension: The role of frictional plastic strain softening inferred from numerical experiments. *Geology*, *30*, 211–214.

Jirásek, M., & Grassl, P. (2008). Evaluation of directional mesh bias in concrete fracture simulations using continuum damage models. *Engineering Fracture Mechanics*, *75*(8), 1921–1943.

Kaus, B. J. P. (2010). Factors that control the angle of shear bands in geodynamic numerical models of brittle deformation. *Tectonophysics*, *484*, 36–47.

Lavier, L. L., Buck, W. R., & Poliakov, A. N. B. (1999). Self-consistent rolling-hinge model for the evolution of large-offset low-angle normal faults. *Geology*, *27*, 1127–1130.

Le Pourhiet, L. (2013). Strain localization due to structural softening during pressure sensitive rate independent yielding. *Bulletin de la Socié‚té géologique de France*, *184*(4-5), 357–371.

Lemiale, V., Mühlhaus, H. B., Moresi, L., & Stafford, J. (2008). Shear banding analysis of plastic models formulated for incompressible viscous flows. *Physics of the Earth and Planetary Interiors*, *171*, 177–186.

Lemonds, J., & Needleman, A. (1986). Finite element analyses of shear localization in rate and temperature dependent solids. *Mechanics of Materials*, *5*, 339–361.

Moresi, L., Mühlhaus, H. B., Lemiale, V., & May, D. A. (2007). Incompressible viscous formulations for deformation and yielding of the lithosphere. *Geological Society, London, Special Publications*, *282*, 457–472.

Mühlhaus, H. B., & Vardoulakis, I. (1987). The thickness of shear bands in granular materials. *Géotechnique*, *37*, 271–283.

Nadai, A. (1931). *Plasticity*. New York: McGraw-Hill.

Needleman, A. (1988). Material rate dependence and mesh sensitivity in localization problems. *Computer Methods in Applied Mechanics and Engineering*, *67*, 69–85.

Niazi, M. S., Wisselink, H. H., & Meinders, T. (2013). Viscoplastic regularization of local damage models: Revisited. *Computational Mechanics*, *51*(2), 203–216.

Olive, J.-A., Behn, M. D., Mittelstaedt, E., Ito, G., & Klein, B. Z. (2016). The role of elasticity in simulating long-term tectonic extension. *Geophysical Journal International*, *205*, 728–743.

Pamin, J., Askes, H., & de Borst, R. (2003). Two gradient plasticity theories discretized with the element-free Galerkin method. *Computer Methods in Applied Mechanics and Engineering*, *192*, 2377–2403.

Peirce, D., Asaro, R. J., & Needleman, A. (1983). Material rate dependence and localized deformation in crystalline solids. *Acta Metallurgica*, *31*, 1951–1076.

Perić, D., Yu, J., & Owen, D. R. J. (1994). On error estimates and adaptivity in elastoplastic solids: Applications to the numerical simulation of strain localization in classical and Cosserat continua. *International Journal for Numerical Methods in Engineering*, *37*, 1351–1379.

Perzyna, P. (1966). Fundamental problems in viscoplasticity. In G. G. Cherny (Ed.), *Recent Advances in Applied Mechanics* (Vol. 9, pp. 243–377). New York: Academic Press.

Poliakov, A. N. B., Herrmann, H. J., Yu, P. Y., & Roux, S. (1994). Fractal plastic shear bands. *Fractals*, *02*(04), 567–581.

Poliakov, A., Podladchikov, Y., & Talbot, C. (1993). Initiation of salt diapirs with frictional overburdens: Numerical experiments. *Tectonophysics*, *228*(3), 199–210.

Popov, A. A., & Sobolev, S. V. (2008). SLIM3D: A tool for three-dimensional thermomechanical modeling of lithospheric deformation with elasto-visco-plastic rheology. *Physics of the Earth and Planetary Interiors*, *171*, 55–75.

Précigout, J., & Gueydan, F. (2009). Mantle weakening and strain localization: Implications for the long-term strength of the continental lithosphere. *Geology*, *37*, 147–150.

Read, H. E., & Hegemier, G. A. (1984). Strain softening of rock, soil and concrete—A review article. *Mechanics of Materials*, *3*, 271–294.

Regenauer-Lieb, K., Poulet, T., Veveakis, M., & Alevizos, S. (2018). The dynamics of multiscale, multiphysics faults: Part I—The long-term behaviour of the lithosphere. *Tectonophysics*, *746*, 648–658. understanding geological processes through modelling - A Memorial Volume honouring Evgenii Burov.

Rudnicki, J. W., & Rice, J. R. (1975). Conditions for the localization of deformation in pressure sensitive dilatant materials. *Journal of the Mechanics and Physics of Solids*, *23*, 371–394.

Sabet, S. A., & de Borst, R. (2019). Structural softening, mesh dependence, and regularisation in non-associated plastic flow. *International Journal for Numerical and Analytical Methods in Geomechanics*, *43*, 2170–2183.

Schmalholz, S. M., Duretz, T., & Jaquet, Y. (2015). Dramatic effect of elasticity on thermal softening and strain localization during lithospheric shortening. *Geophysical Journal International*, *204*, 780–784.

Sluys, L. J., & Berends, A. H. (1998). Discontinuous failure analysis for mode-I and mode-II localization problems. *International Journal of Solids and Structures*, *35*(31), 4257–4274.

Sluys, L. J., & de Borst, R. (1992). Wave propagation and localization in a rate-dependent cracked medium—Model formulation and one-dimensional examples. *International Journal of Solids and Structures*, *29*, 2945–2958.

Spiegelman, M., May, D. A., & Wilson, C. R. (2016). On the solvability of incompressible stokes with viscoplastic rheologies in geodynamics. *Geochemistry, Geophysics, Geosystems*, *17*, 2213–2238. https://doi.org/10.1002/2015GC006228

Stefanou, I., Sulem, J., & Rattez, H. (2019). Cosserat approach to localization in geomaterials. In G. Z. Voyiadjis (Ed.), *Handbook of Nonlocal Continuum Mechanics for Materials and Structures* (pp. 1–25). Berlin: Springer.

Tackley, P. J. (2000). Self-consistent generation of tectonic plates in time-dependent, three-dimensional mantle convection simulations 2. Strain weakening and asthenosphere. *Geochemistry, Geophysics, Geosystems*, *1*(8), 1026. https://doi.org/10.1029/2000GC000043

Thielmann, M., & Kaus, B. J. P. (2012). Shear heating induced lithospheric-scale localization: Does it result in subduction? *Earth and Planetary Science Letters*, *359*, 1–13.

Vermeer, P. A., & de Borst, R. (1984). Non-associated plasticity for soils, concrete and rock. *Heron*, *29*(3), 3–64.

Wang, K. (2007). Elastic and viscoelastic models of crustal deformation in subduction earthquake cycles. In T. Dixon, & J. C. Moore (Eds.), *The seismogenic zone of subduction thrust faults* (pp. 540–575). New York: Columbia University Press.

Wang, W. M., Sluys, L. J., & de Borst, R. (1996). Interaction between material length scale and imperfection size for localisation phenomena in viscoplastic media, European. *Journal of Mechanics. A, Solids*, *15*, 447–464.

Wang, W. M., Sluys, L. J., & de Borst, R. (1997). Viscoplasticity for instabilities due to strain softening and strain-rate softening. *International Journal for Numerical Methods in Engineering*, *40*(20), 3839–3864.

Willett, S. D. (1992). Dynamic and kinematic growth and change of a Coulomb wedge. In K. R. McClay (Ed.), *Thrust Tectonics* (pp. 19–31). Dordrecht: Springer.

Yin, A., Xie, Z., & Meng, L. (2018). A viscoplastic shear-zone model for deep (15–50 km) slow-slip events at plate convergent margins. *Earth and Planetary Science Letters*, *491*, 81–94.